

Journal of Biomedical Optics

BiomedicalOptics.SPIEDigitalLibrary.org

Nonconfocal all-optical laser- ultrasound and photoacoustic imaging system for angle-dependent deep tissue imaging

Jami L. Johnson
Jeffrey Shragge
Kasper van Wijk

SPIE.

Jami L. Johnson, Jeffrey Shragge, Kasper van Wijk, "Nonconfocal all-optical laser-ultrasound and photoacoustic imaging system for angle-dependent deep tissue imaging," *J. Biomed. Opt.* **22**(4), 041014 (2017), doi: 10.1117/1.JBO.22.4.041014.

Nonconfocal all-optical laser-ultrasound and photoacoustic imaging system for angle-dependent deep tissue imaging

Jami L. Johnson,^{a,*} Jeffrey Shragge,^b and Kasper van Wijk^a

^aUniversity of Auckland, Faculty of Science, The Dodd-Walls Centre for Photonic and Quantum Technologies and Department of Physics, Private Bag 92019, Auckland 1010, New Zealand

^bThe University of Western Australia, Faculty of Science, School of Physics and School of Earth Sciences, M004 35 Stirling Highway, Crawley, Western Australia 6009, Australia

Abstract. Biomedical imaging systems incorporating both photoacoustic (PA) and ultrasound capabilities are of interest for obtaining optical and acoustic properties deep in tissue. While most dual-modality systems utilize piezoelectric transducers, all-optical systems can obtain broadband high-resolution data with hands-free operation. Previously described reflection-mode all-optical laser-ultrasound (LUS) systems use a confocal source and detector; however, angle-dependent raypaths are lost in this configuration. As a result, the overall imaging aperture is reduced, which becomes increasingly problematic with depth. We present a reflection-mode nonconfocal LUS and PA imaging system that uses signals recorded on all-optical hardware to create angle-dependent images. We use reverse-time migration and time reversal to reconstruct the LUS and PA images. We demonstrate this methodology with both a numerical model and tissue phantom experiment to image a steep-curvature vessel with a limited aperture 2-cm beneath the surface. Nonconfocal imaging demonstrates improved focusing by 30% and 15% compared to images acquired with a single LUS source in the numerical and experimental LUS images, respectively. The appearance of artifacts is also reduced. Complementary PA images are straightforward to acquire with the nonconfocal system by tuning the source wavelength and can be further developed for quantitative multiview PA imaging. © 2017 Society of Photo-Optical Instrumentation Engineers (SPIE) [DOI: [10.1117/1.JBO.22.4.041014](https://doi.org/10.1117/1.JBO.22.4.041014)]

Keywords: photoacoustic imaging; laser-ultrasound; all-optical; time reversal; reverse-time migration.

Paper 160564SSPRR received Aug. 24, 2016; accepted for publication Jan. 3, 2017; published online Jan. 26, 2017.

1 Introduction

Acoustic waves are weakly scattered and absorbed in biological tissue¹ and are therefore useful for biomedical imaging. Both photoacoustic (PA) and ultrasonic imaging harness these characteristics, but toward different ends.² A PA source is generated by sending a nanosecond pulse of light into biological tissue. The light is absorbed by tissue chromophores beneath the surface, causing a rapid temperature increase. The corresponding thermoelastic expansion generates a pressure wave originating at the location where the light is absorbed. The goal of PA imaging is to locate these embedded sources and quantify the strength of absorption using data recorded at the surface. On the other hand, ultrasonic imaging aims to detect and image acoustic scatterers by mapping the origin of acoustic wavefield changes due to scattering, reflection, and/or refraction from discontinuities in the acoustic refractive index.

PA and ultrasonic imaging provide complementary information about tissue properties,² so dual-modality systems incorporating both types of imaging and analyses are desirable. Several dual PA and ultrasonic systems have been demonstrated, most commonly utilizing piezoelectric transducers for ultrasonic generation as well as detection of the ultrasound and PA waves.^{3,4} Piezoelectric transducers have narrow frequency bandwidths

and are, therefore, not ideal for detecting inherently broadband PA waves. Furthermore, transducers exhibit a tradeoff between sensitivity and element size (putting an upper limit on lateral resolution) and require contact with the sample and an acoustic coupling medium. In contrast, optical detectors for PA imaging have obtained high sensitivity, optical diffraction-limited resolution, and broad frequency bandwidths. A limited list of these detectors includes optical interferometers,⁵⁻⁷ Fabry-Pérot detectors,⁸ microring resonators,⁹ Fiber Bragg sensors,¹⁰ and optical beam deflection techniques.¹¹⁻¹³ For ultrasonics, the PA effect has been harnessed to induce laser-ultrasound (LUS) generation at the tissue surface.¹⁴⁻¹⁷ The resulting wavelets can achieve wide frequency bandwidths without ringing.¹⁸ Overall, purely optical systems allow for broadband PA and ultrasonic images to be obtained. The only difference in acquiring each of the wavefields is tuning where the acoustic waves are generated. Additionally, all-optical systems open up applications where contact with the sample and manual manipulation of a probe is harmful (as for burned tissue) or inconvenient (such as surgical guidance).

Both transmission¹⁴ and reflection mode^{6,15,16} LUS systems have been described, with reflection mode being most practical for clinical applications in which access is limited to a single side of the tissue. Additionally, the penetration depth of light is limited to a few centimeters in tissue for PA imaging, so

*Address all correspondence to: Jami L. Johnson, E-mail: jami.johnson@auckland.ac.nz

reflection mode is preferred for systems incorporating both modalities. However, a major challenge of reflection-mode systems is the limited imaging aperture. To the authors' knowledge, every reflection-mode LUS system incorporating all-optical hardware utilizes confocal sources and receivers, where the wavefield is both generated and detected at a single point. Two-dimensional (2-D) volumes are then generated by scanning the sample.^{6,19}

In this work, we present an alternative nonconfocal approach. We utilize the term "nonconfocal" to indicate acquisition of independent information about each source–receiver pair. Specifically, for each localized light-pulse that is triggered, a line of receivers records the resulting wavefield. This multiview approach has shown to be advantageous for obtaining unique source distributions for quantitative PA imaging.^{20,21} However, the advantages of nonconfocal acquisition for all-optical LUS systems have not been studied previously.

One advantage of nonconfocal all-optical acquisition is the increased suitability for powerful wave-equation-based reconstruction methods. Time-reversal has been studied extensively^{22–27} and is described as the most versatile imaging approach for PA imaging²⁸ since both acoustic heterogeneity^{26,28,29} and acoustic absorption³⁰ can be incorporated. Similarly, reverse-time migration (RTM) is a wave-equation-based reconstruction method that has shown to be powerful in both seismic imaging^{31,32} and ultrasonics.^{33,34} Nonetheless, ray-based imaging techniques, such as delay-and-sum algorithms,³⁵ synthetic aperture focusing,³⁶ and Kirchhoff migration are most commonly used for medical ultrasonics. Ray-based methods work fairly well on sparse or irregularly sampled data and are thus well suited to ultrasound data recorded by transducers. However, ray-based solutions deteriorate in the presence of sharp discontinuities in acoustic impedance (e.g., near bone). This is due to significant angular deviation occurring at discontinuities due to a small perturbation in ray angle. Unlike ray-based techniques, RTM based on finite-difference solutions to the acoustic wave equation naturally handles multipathing from strong discontinuities and allows for a frequency-dependent response, but relies on densely sampled wavefields. Therefore, a nonconfocal all-optical system can harness the full resolution power of RTM.

The primary advantage we demonstrate is the angle-dependent information that is obtained by nonconfocal laser-ultrasonics, specifically. The limited aperture problem increases with depth in ultrasonics. Significant advancements have been made in the transducer-based ultrasonics community to insonify tissue from various angles to obtain angle-dependent images, which are stacked to obtain a final image with an increased aperture and reduced artifacts.³⁷ Likewise, synthetic aperture imaging uses nonconfocal, unfocused transmit elements and focused receive elements to reconstruct higher resolution images.³⁶ In the same way, we use nonconfocal LUS to probe the tissue from multiple directions. For a confocal source and detector, we have information about acoustic propagation only along a single A-line; however, when the wavefield is recorded at many detector positions for a single LUS source, we record angle-dependent raypaths. The combination of nonconfocal laser-ultrasonics with RTM is well suited for imaging structures with steep curvature that are difficult to image with a limited aperture. The combined methodology improves the effective imaging aperture and allows the advantages of spatial compounding to be exploited. Multiple angles of insonification are also important for imaging of anisotropic tissue such as

muscle and tendon, where anisotropy can be mistaken for pathology.³⁸ Therefore, angle-dependent imaging will likely be necessary in order for reflection-mode LUS to find application clinically.

In the following sections, we first present a numerical model that demonstrates the advantages of angle-dependent illumination for LUS in a model with high acoustic contrast and steep curvature. Subsequently, we describe our nonconfocal all-optical PA and LUS imaging system that demonstrates these advantages for all-optical LUS for the first time experimentally. Multiview PA data can be obtained with the same system as the nonconfocal LUS by tuning only the location where acoustic generation occurs. The main contribution of this work is the use of angle-dependent information from an all-optical LUS system. At the same time, we incorporate the known advantages of all-optical reflection-mode PA and LUS imaging, wave-equation-based reconstruction, and multiview PA imaging.

2 Methods

2.1 Numerical Model

To illustrate the advantages of nonconfocal laser-ultrasonics, we create a 2-D acoustic numerical model that simulates the acoustic properties of biological tissue. We use Gmsh meshing software³⁹ to create a second-order (curvilinear) quadrilateral mesh, with a circular vessel with high contrast walls 2-cm deep in a homogeneous background medium. Figures 1(a) and 1(b) show the dimensions of the model, whereas Table 1 lists the acoustic properties. The acoustic properties of the vessel wall are in the range of a calcified blood vessel.^{40,41} The imaging aperture is limited to about 53 deg, which is too narrow to image the full circumference of the steep curvature of the model vessel. While recording the wavefield on multiple sides of the model would improve the aperture, the goal of this work is to address situations in which reflection-mode is necessary.

We simulate the LUS source as a 2-MHz first-derivative Gaussian wavelet and numerically propagate the wavefield through the model using the SPEC-FEM2D⁴² solver. We place a total of 16 equally spaced ultrasound sources across 2 cm of the surface. Each independently fired source emits a "source" wavefield that propagates into the phantom interior and is then scattered by the vessel. The scattered wavefield is subsequently detected by 101 displacement detectors at the surface. This method of firing each source individually and recording the response by an array of detectors in reflection-mode is known as a "common source gather" in seismic imaging terminology.⁴³

As required by SPEC-FEM2D, we model the PA source as a uniform distribution of 242 PA point-sources inside of the circular vessel. The PA source term is defined as the derivative of the temporal and spatial source distribution [see Eq. (1) in Appendix A1]. As quantitative PA imaging is outside of the scope of this work and described elsewhere,^{20,21} we do not model the source distribution for light illuminated from each source position. We assume each point source undergoes Gaussian heating and, therefore, we model the source wavelet as a first-derivative Gaussian. The central frequency of the wavelet is chosen to be 2 MHz, such that the wavelength is approximately half of the vessel diameter. We fire all sources simultaneously, and the superposition of the waves propagates as a PA wavefield that is detected by the same array of 101 displacement detectors at the surface.

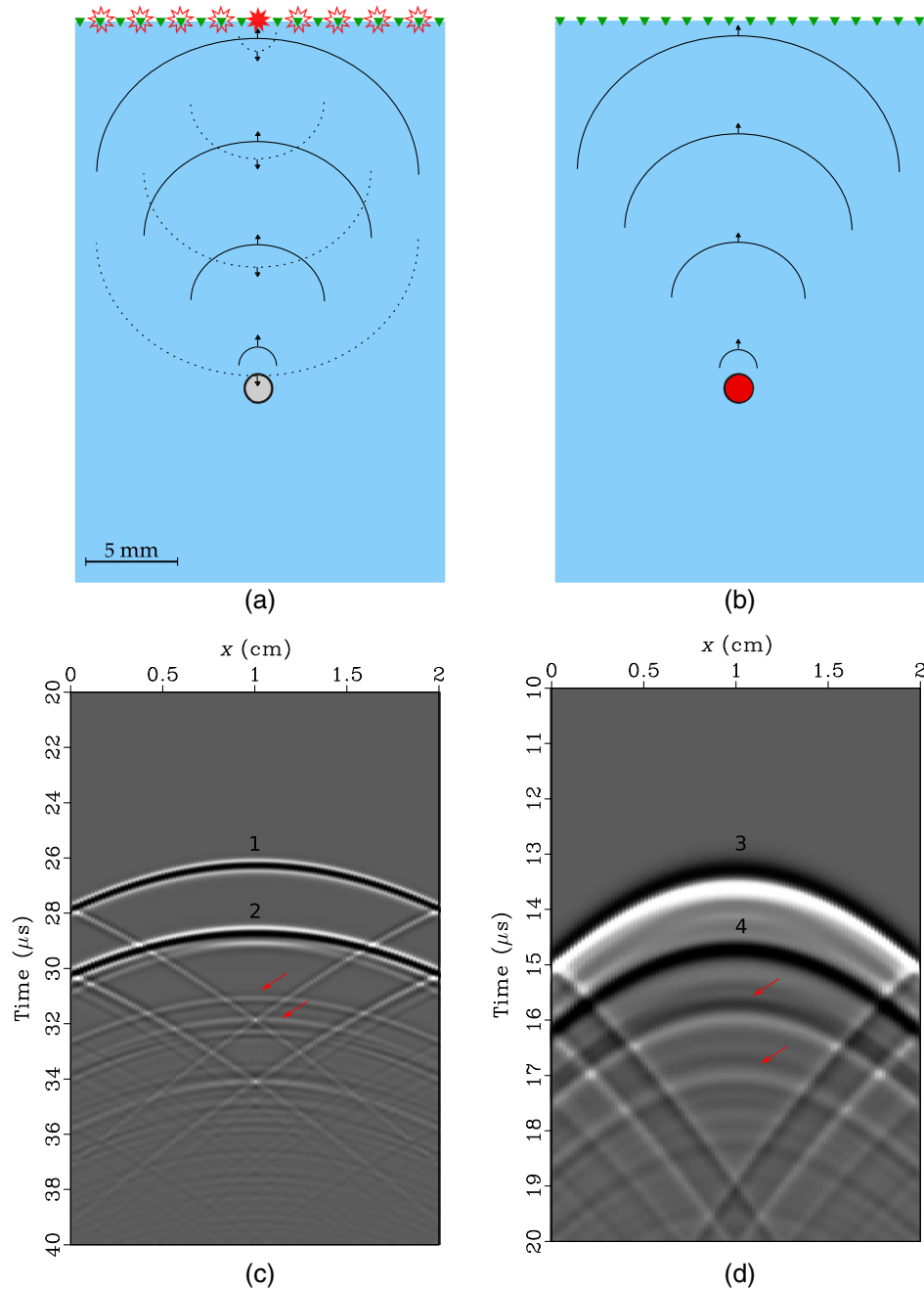


Fig. 1 Schematic diagram of vessel embedded in tissue phantom used for simulating propagation of (a) LUS and (b) PA waves with SPEC-FEM2D. Sources are outlined in red, and detectors are green. The active LUS source is indicated by the filled red source. In the LUS model, the solid line represents the scattered wavefield. The data extracted at the surface by the detectors $\mathcal{D}(x, z = 0, t)$ are shown for the (c) LUS and (d) PA models. (1) and (2) denote the arrival of the LUS waves scattered off of the top and bottom walls of the vessel, and (3) and (4) are the PA waves generated at the top and bottom walls of the vessel, respectively. Multiple reflections are indicated by red arrows.

Table 1 Acoustic properties used for numerical model.

Medium	Density (kg/m ³)	Velocity (ms ⁻¹)
Background	1000	1500
Vessel interior	768	1170
Vessel wall	1180	2740

2.2 Experimental Methods

We show the nonconfocal all-optical experimental setup in Fig. 2. We mount an optical vibrometer (OFV-505, Polytec, Irvine, California) on a linear stage (M-IMS300LM, Newport, Irvine, California) to detect the acoustic waves. A Nd:YAG laser generates a 10-ns pulse with a 10-Hz repetition rate. The 1064-nm beam is collimated with a 8-mm diameter and has a pulse energy of 100 mJ/cm², which is below the maximum permissible exposure for biological tissue at 1064 nm.⁴⁴

The source beam is directed toward the sample by a mirror mounted on a rotation stage (URS1000BCC, Newport). The source is offset 5 mm from the detection beam in the plane out of the page in Fig. 2.

We create a solid tissue phantom with analogous acoustic properties to those used in the numerical model above. The phantom is composed of 1% Intralipid (Fresenius Kabi, Uppsala, Sweden) and 1% agar (A0930-05, U.S. Biological, Swampscott, Massachusetts).⁴⁵ The phantom vessel is an acrylic tube with an inner diameter of 1.4 mm and wall thickness of $233.5 \mu\text{m}$ as the phantom vessel. The vessel is filled with infrared absorbing dye (Epolight 2057, Epolin, Newark, New Jersey, $\mu_a \approx 30 \text{ cm}^{-1}$) and embedded 2 cm under the acquisition surface.

We perform two experiments to obtain multiview PA and nonconfocal LUS data. First, we place a retroreflective tape across the detection line only, such that the source laser beam is directly incident on the phantom tissue. In this configuration, PA generation dominates, and the LUS generation at the surface is minimal. Second, we extend the tape across the source line. In that case, a majority of the incident source light is absorbed by the tape at the surface; therefore, a strong LUS wave is generated while minimizing PA generation. We note that instead of incorporating an absorbing layer at the surface, the wavelength of the source can be tuned to obtain strong absorption by the tissue surface itself. For example, the wavelength can be tuned to an absorption peak for melanin or water² to generate LUS superficially. At many wavelengths, both PA and LUS generation occur. In such cases, LUS and PA datasets can be acquired from a single scan by isolating each wavefield with a simple time gate. This is a practical approach for media with low acoustic heterogeneity, but will degrade in complex

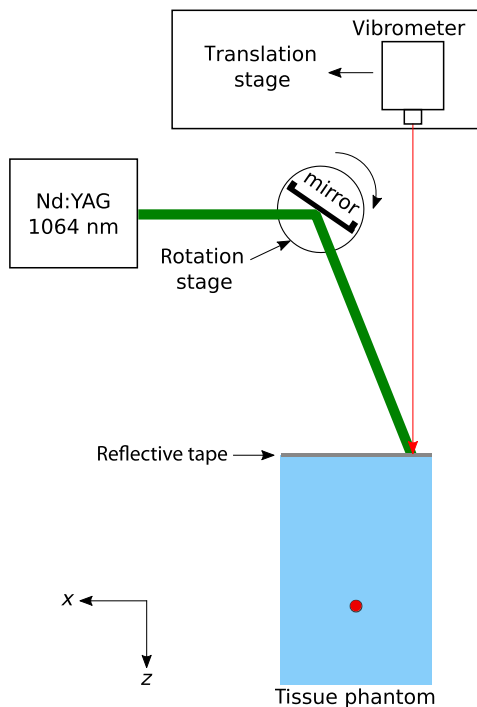


Fig. 2 Experimental setup for PA and LUS experiment. We use a nonconfocal all-optical acquisition system to scan an Intralipid and agar tissue phantom with a phantom vessel embedded 2-cm deep. The vessel contains optically absorbing dye and a wall with high acoustic contrast.

tissue where the wavefields overlap in time. A more advanced method requires a modeling operator to simultaneously model both PA and LUS signals. Then, a joint inversion procedure could be used to find the range of physical model parameters that explain the observations. However, this is beyond the scope of this paper.

We record 17 scans in each configuration. For each scan, the source beam is kept at a single and unique surface location. We scan the vibrometer across 2 cm of the surface in the x -direction and record the average of 64 waveforms at a $\Delta x = 200 \mu\text{m}$ increment. Then, we rotate the mirror such that the source beam moves 1.25 mm in the x -direction, and we repeat the vibrometer scan. This iterative process is continued for all 17 source positions. Previously described reflection-mode all-optical systems use a confocal source and detector, whereas we acquire each source–detector pair sequentially. Therefore, we can obtain angle-dependent all-optical LUS images by utilizing the information about raypaths between each source and detector position. Furthermore, our nonconfocal strategy creates a slightly different PA light distribution for each source position, which is recorded by all detectors. We automate the experiment and data acquisition with Python using the open-source PLACE software package.⁴⁶

To further isolate the PA and LUS wavefields, we apply a weighted subtraction between the corresponding scans from each configuration. The processed and highpass filtered (100 kHz) data are shown in Fig. 3.

2.3 Image Reconstruction

We use time reversal and RTM to reconstruct the PA and LUS images, respectively. For the interested reader, we provide a detailed outline of the reconstruction algorithms in Appendix A1 and A2. For the PA reconstruction, we stack the data from all scans before image reconstruction, while the LUS images are stacked after reconstruction of images from each independent source for spatial compounding.

The use of ultrasound to obtain acoustic properties of the medium for the PA reconstruction is continually under

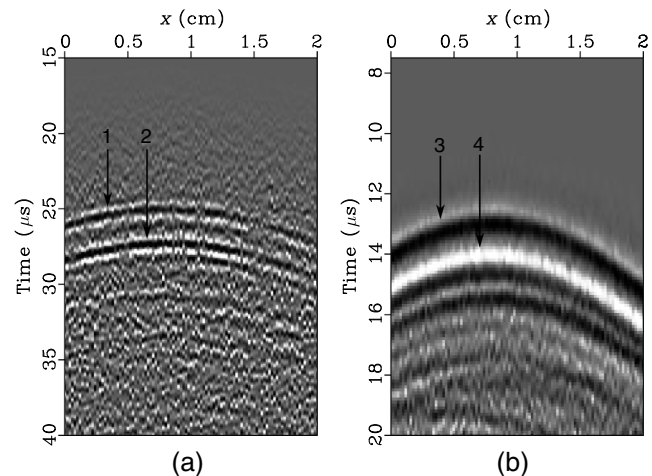


Fig. 3 Experimental (a) LUS and (b) PA wavefields. (1) and (2) denote the arrival of the LUS waves scattered off of the top and bottom walls of the phantom vessel, and (3) and (4) are the PA waves generated at the top and bottom walls of the vessel, respectively. The PA wavefield is the stacked data from every scan. Surface waves are muted in both (a) and (b).

investigation.^{15,47–49} However, this approach is most effective with full-field data and degrades as the imaging aperture is reduced (as in deep tissue reflection-mode imaging). Therefore, for our reflection-mode system, we have opted to use a homogeneous and lossless background medium for both the PA and LUS reconstruction.

3 Results

3.1 Numerical Results

In Fig. 4, we show the reconstructed individual-source (a) and compound (stacked) image in (b) for the LUS model. Multiple reflections within the vessel propagate along different raypaths and map to a slightly different location depending on the position of the original source. Therefore, these artifacts sum destructively, whereas the direct reflections from the vessel wall sum constructively. The curvature of the vessel is more accurately represented in the compound image, because angle-dependent information is obtained from the images formed from each source. There is also a clear improvement in overall focusing (lateral resolution). We observe a 30% decrease in the apparent vessel width in the compound image, measured as

the width of the bottom wall. The appearance of artifacts is reduced by stacking of artifacts produced from different angles.

The PA image is shown in Fig. 4(c). The initial PA pressure distribution (the “source signature”) is a complicated shape due to the strong acoustic contrast surrounding the optical absorber. For the purposes of imaging and interpretation, it is beneficial to remove the source signature and produce an image that is representative of the overall source energy. Here, we apply a Hilbert transform⁵⁰ to obtain the complex analytical representation of the real image. Subsequently, we take the power spectra of this data, which is proportional to the energy of the source, as shown in Fig. 4(d).

3.2 Experimental Results

The experimental LUS image for a single scan and compound image from all 17 scans are shown in Figs. 5(a) and 5(b), respectively. The compound image shows improved focusing (15%) compared to the single-source image, as measured by the width of the bottom wall of the vessel in Figs. 5(a) and 5(b). Limited-view and reverberation artifacts are reduced by stacking images acquired from each angle in Fig. 5(b) compared to the image from a single source in (a). The artifacts would be further

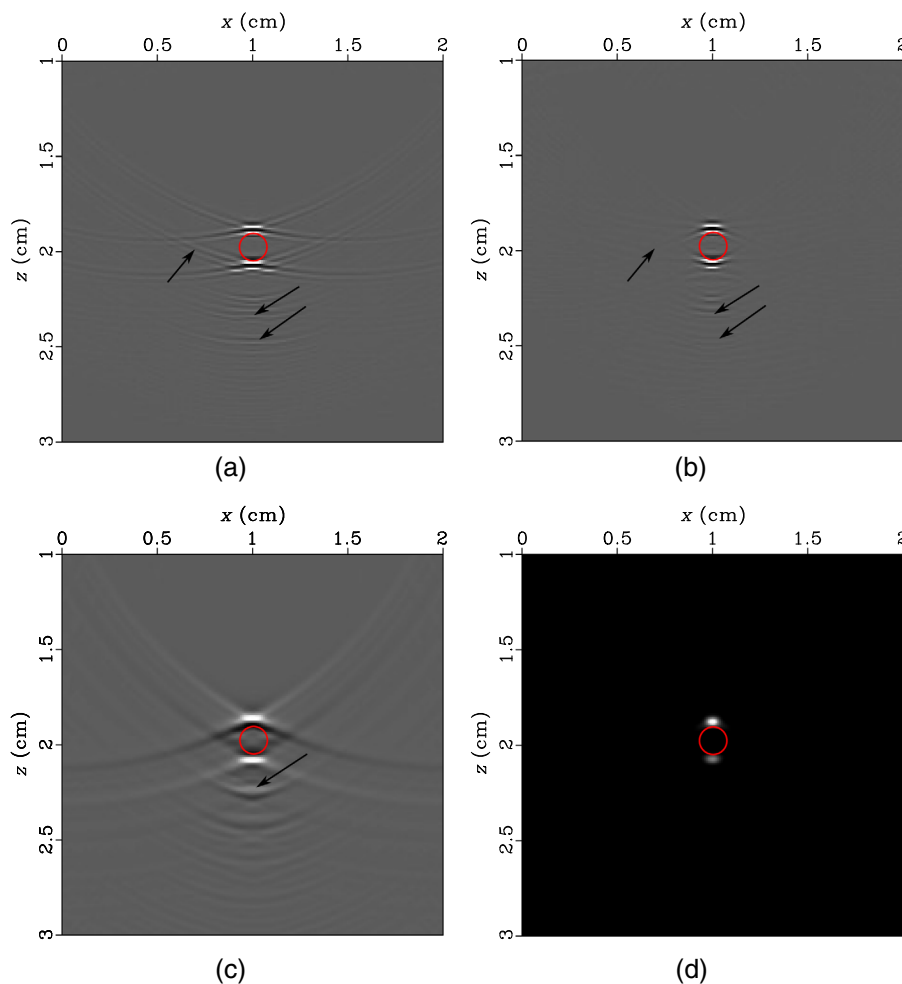


Fig. 4 Imaging results for numerical data with the inner diameter of the vessel model overlaid in red. The LUS image is created using (a) a single source and (b) multiple sources. The PA image is shown in (c), and the power spectrum of the Hilbert-transformed PA image is in (d). Arrows indicate artifacts, which are reduced in the multiple-source LUS image and processed PA image.

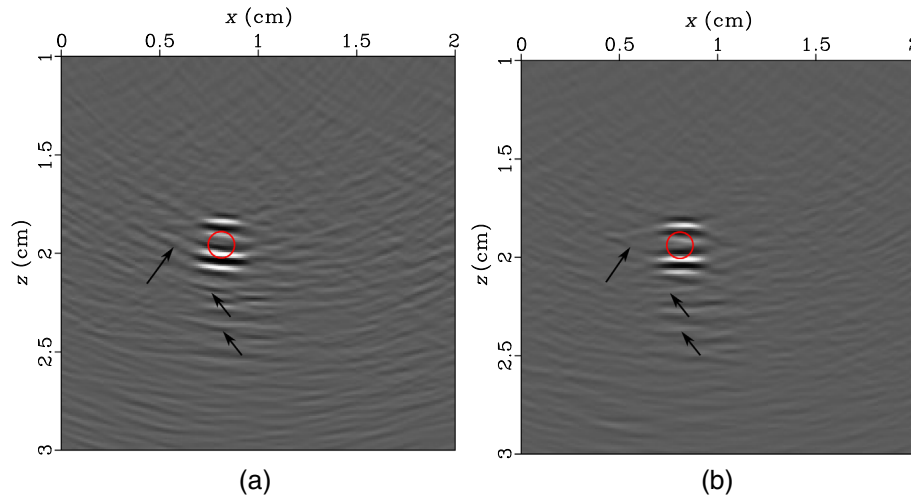


Fig. 5 LUS images for experimental data. The LUS image using a single scan (with a single source position) is shown in (a) and the stacked image formed from all 17 LUS scans are shown in (b). The inner diameter of the vessel is indicated in red. Arrows indicate artifacts in (a) that are effectively suppressed in (b).

suppressed by using a smaller, more localized spot-size for the source, and using additional source positions. Ideally, one LUS source would be used for each detection point. Reverberations in the PA data are mapped to the wrong location [Figs. 6(a) and 6(b)]. These artifacts reduce the depth-resolution of the PA image; therefore, the LUS image also helps to interpret the true structure of the target. The power spectrum of the Hilbert-transformed image is shown in Fig. 6(c).

3.3 Dual-Modality Images

Overlaying the PA and LUS images (Fig. 7) demonstrates several advantages of our dual-modality system. First, the two images provide both optical absorption and acoustic scattering information about the medium. In this example, the absorber is an analogue of hemoglobin, whereas the vessel wall can be compared to a stenotic or calcified vessel. Second, the PA image alone could be interpreted as containing two strong absorbers. However, the LUS image elucidates that there is a strong acoustic scatterer in

direct contact with the absorbing molecules, therefore causing stronger generation at this interface. Therefore, the LUS is a complementary modality for interpreting the PA image.

4 Discussion

The combination of PA and LUS imaging provides valuable optical and acoustic information about targets deep within tissue. We have shown that spatial compounding with nonconfocal LUS data improves the focusing power of a limited-aperture system, as quantified by the 30% and 15% reduction in the vessel width numerically and experimentally, respectively. Furthermore, the artifacts are suppressed by image compounding. In both cases, numerical results show greater improvements compared to the experimental results. In the numerical model, we ignore attenuation; therefore, the artifacts due to multiple scattering are stronger than we would expect to be observed in the experimental data for this model. Additionally, the experimental LUS source has a diameter of 8 mm, thus the resolution of the LUS image

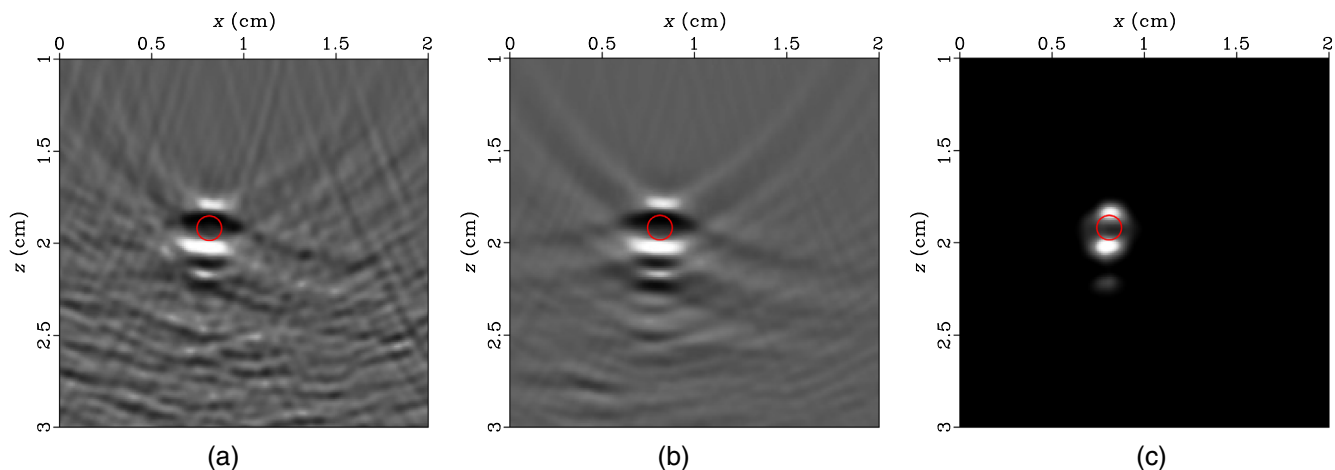


Fig. 6 Experimental PA image reconstructed with time-reversal. The image from a single scan is shown in (a), and the image reconstructed with the stacked PA data is in (b). The power spectrum of the Hilbert-transformed image is shown in (c).

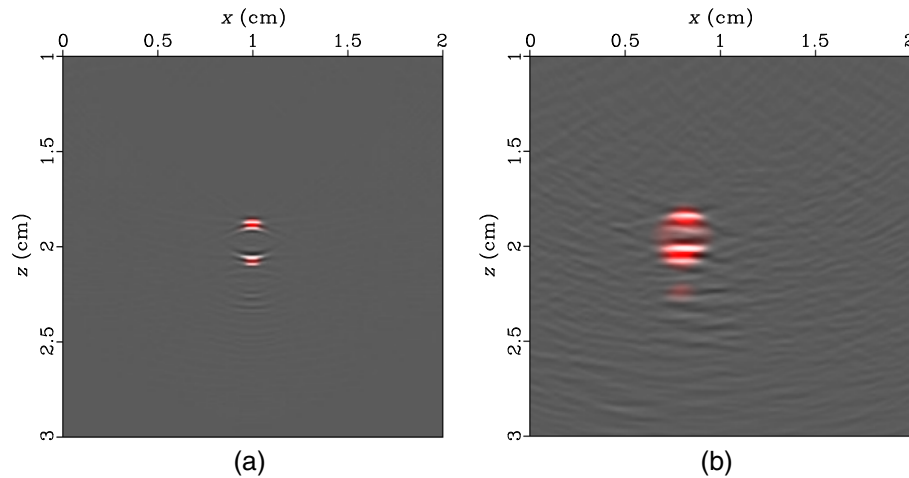


Fig. 7 Overlay of PA (red) and LUS (gray scale) images for (a) numerical model (b) experimental data.

can be further improved by focusing the source to achieve better localization.

In this example, we use only 17 LUS sources, but further improvements in focusing and artifact suppression are expected with additional sources. A limited number of sources is used due to the lengthy acquisition time (about 11 min/source-scan). The scan time is limited by the 10-Hz repetition rate of the source laser and scanning of a single-point detector with 64 averages. Acquisition time can be significantly reduced with parallelized detection and the use of source lasers with faster repetition rates. The reconstruction time is also longer than ray-based techniques, but we expedite reconstruction time by using the finite-difference time-domain (FDTD) method described in Appendix A1. For a 2-D computational grid (384×2000 samples) on a typical single GPU workstation, it takes approximately 2 min to reconstruct the PA image and 2.5 min for the LUS reconstruction corresponding to one source. These times could be significantly reduced by the utilization of parallelized GPUs within a single work station. The advantages of nonconfocal imaging can still be applied to reconstruction with straight-ray methods to expedite reconstruction. Full-wavefield methods are more computationally complex, but also more accurate than straight-ray methods in complex imaging scenarios. Therefore, the proposed reconstruction methods lead toward quantitative imaging methods from which diagnostically relevant physical parameters can be extracted.

The single-pulse energy in these experiments is within the laser safety limits for biological tissue. However, the number of averages and energy density would require optimization to remain safe for clinical application. The largest contribution to energy exposure is repeated source generation in the same location for each detection point. Parallelized detection would substantially reduce the energy exposure for each source position.

In this demonstration, we focus on a model with acoustic contrast and steep curvature that demonstrates the primary advantages of nonconfocal LUS for deep tissue imaging. RTM is also well suited for this model, but would be further exploited in a model with stronger heterogeneities present, such as bone.

The PA image reconstructed from the sum of all 17 PA scans also shows improved signal-to-noise compared to the image created from illumination from a single direction. Multiview illumination creates a slightly different PA source distribution and suppresses incoherent noise. In both the numerical and

experimental results, strong acoustic generation is observed at the vessel walls. This is caused by the high acoustic contrast between the dye and vessel wall, and destructive interference occurring between the interior sources. The frequency content (and therefore resolution) is dictated by the dimension of the absorber in the direction of propagation. For the PA wavefield, this is the inner diameter of the vessel (1.4 mm). In LUS, the frequency is dictated by the effective skin-depth,⁵¹ which is on the order of hundreds of micrometers for excitation on our opaque tape. To increase the PA frequency in the phantom vessel and also decrease the destructive interference between interior sources, we can decrease the effective size of the absorbers by using dynamic speckle illumination.⁵²

5 Future Work

There are several extensions of the current system and methods that can build upon the work presented. First, the artifacts are adequately suppressed in the LUS image, but are not considered in the current PA reconstruction. We use a uniform background velocity, thus the PA artifacts are due to multiple reflections by the vessel wall that are not accounted for in the background model. A variable-density acoustic wave equation could be used to reconstruct the PA image if the acoustic properties in the medium are extracted using quantified RTM data and then incorporated into the numerical model for PA reconstruction. As the conventional approach to incorporating acoustic heterogeneities into the PA background degrades as the imaging aperture is reduced, future work will focus on suppressing multiple-reflections from reflection-mode data using Marchenko redatuming.⁵³

Second, attenuation is ignored in this implementation, but must be considered for quantitative imaging (i.e., inversion). We note that the above approach could be extended to account for the attenuation by implementing a visco-acoustic least-squares RTM to both estimate the quality-factor (Q) and acoustic index of refraction.⁵⁴

Third, for true amplitude (quantitative) imaging with RTM, the light distribution in the tissue must be known. Therefore, a further extension for RTM is to model the light distribution and compute the source signature $[\partial h(x, z, t)/\partial t]$ in Eq. (1) of Appendix A1]. Then, the LUS source wavelet can be accurately modeled and the integral of the wavelet can be used for the source wavefield in RTM.⁵⁵ Likewise, the light distribution must

be known or accurately estimated for quantitative PA imaging.⁵⁶ Nonetheless, illumination from multiple directions allows a straightforward path to quantitative PA tomography.^{20,21}

Finally, several methods exist for removing the source signature of time-reversed images. We present a simple example using the Hilbert transform for the PA image, but more sophisticated methods of obtaining the optimal signal for time reversal, such as multidimensional source deconvolution,⁵⁷ are expected to improve the result.

6 Conclusions

We describe a nonconfocal all-optical LUS and PA system that obtains angle-dependent, high-resolution data with a broad frequency bandwidth. In the proposed system, images of both acoustic and optical properties are obtained with hands-free operation. While multiview imaging for PAs has been demonstrated previously, we demonstrate the advantages of nonconfocal all-optical LUS in both a numerical model and tissue phantom experiment for the first time. For the deep, steep-curvature vessel model presented, we show that nonconfocal LUS reduces artifacts and improves focusing by 30% and 15% in numerical and experimental images, respectively. The approach described is a step toward quantitative, high-resolution imaging when combined with the proposed wave-equation-based imaging techniques and modeling of the optical source distribution. In the presence of strong acoustic scattering (e.g., bone), the full power of RTM with such a nonconfocal system is expected to demonstrate even greater improvements.

Appendix

A1 Generating Solutions to the Acoustic Wave Equation

The constant density 2-D acoustic wave equation with a laser-generated source term can be written as

$$\left[\frac{1}{v^2(x, z)} \frac{\partial^2}{\partial t^2} - \nabla^2 \right] p(x, z, t) = \Gamma(x, z) \frac{\partial h(x, z, t)}{\partial t}, \quad (1)$$

where $v = v(x, z)$ is the velocity field in the medium in a 2-D Cartesian coordinate system $\mathbf{x} = [x, z]$, $p(x, z, t)$ is the acoustic wavefield, and $\Gamma(x, z)$ is the Grüneisen coefficient of the tissue. The source heating term

$$h(x, z, t) = \mu_a(x, z) \phi(x, z, t) \quad (2)$$

is the spatial and temporal heating of the tissue due to optical absorption, where $\mu_a(x, z)$ is the optical absorption coefficient and $\phi(x, z, t)$ is the light fluence at a location in space and time.⁵⁸

To propagate the acoustic wavefields and solve for $p(x, z, t)$ numerically, we use an $\mathcal{O}(\Delta t^2, \Delta x^8)$ FDTD equation to evolve the discretized wavefield $p_{l,m}^n(l\Delta x, m\Delta z, n\Delta t)$, where (l, m, n) are integer indices of a grid point in the x , z , and t dimension, respectively. We set the source term in Eq. (1) to zero

$$\left[\frac{1}{v^2(x, z)} \frac{\partial^2}{\partial t^2} - \nabla^2 \right] p(x, z, t) = 0, \quad (3)$$

and inject the energy of a wavefield into $p(x, z = 0, t)$ as a boundary condition. Assuming $\Delta x = \Delta z$, we discretize Eq. (3)

Table 2 Finite-difference stencil coefficients of Δx^8 accuracy used in Eq. (4).⁵⁹

Coefficients	c_0	$c_{\pm 1}$	$c_{\pm 2}$	$c_{\pm 3}$	$c_{\pm 4}$
Value	$-\frac{205}{72}$	$\frac{8}{5}$	$-\frac{1}{5}$	$\frac{8}{315}$	$-\frac{1}{560}$

$$p_{l,m}^{n+1} = 2p_{l,m}^n - p_{l,m}^{n-1} + \frac{\Delta t^2 v^2}{\Delta x^2} \sum_{i=-4}^{i=4} c_i (p_{l+i,m}^n + p_{l,m+i}^n), \quad (4)$$

where $c_i = c_{-i}$, with values given in Table 2. This formula emerges by solving a Taylor-series expansion to the eighth-order in space and second-order in time about $p_{l,m}^n$ to solve for $\nabla^2 p$ and $\partial^2 p / \partial t^2$, respectively. These derivatives are substituted into Eq. (3) to arrive at the update equation for forward step $p_{l,m}^{n+1}$ [Eq. (4)]. Note that to obtain the summation term with coefficients c_i on the right-hand side of Eq. (4), the spatial Taylor series is computed for $p_{l+i,m}^n$ and $p_{l,m+i}^n$ for $-4 \leq i \leq 4$. The FDTD algorithm is implemented with a GPU-based stencil approach. The memory and speed advantages of this technique are described by Weiss and Shragge.⁶⁰

A1.1 Ultrasound Reconstruction and Imaging with Reverse-Time Migration

The key principle of RTM is based on Huygens' principle, which states that at the instant in time when an acoustic

Algorithm 1 RTM for nonconfocal ultrasound.

```

1: for all ultrasound sources do
2:   Generate numerical approximation of the ultrasound wavelet
3:   Initialize  $\mathcal{S}(x, z, t - \Delta t) = 0$ 
4:   for  $t_0 < t < t_{\max}$  do
5:     Inject source wavelet energy into  $\mathcal{S}(x, z, t)$ 
6:     Construct  $\mathcal{S}(x, z, t + \Delta t)$  from  $\mathcal{S}(x, z, t)$  and  $\mathcal{S}(x, z, t - \Delta t)$ 
7:   end for
8:   Time-reverse  $\mathcal{S}(x, z, t)$  at  $t_{\max}$ 
9:   Reverse-time axis of ultrasound data  $\mathcal{D}^\dagger(x, t)$ 
10:  Initialize  $\mathcal{R}^\dagger(x, z, t_{\max} + \Delta t) = 0$ 
11:  for  $t_{\max} > t > t_0$  do
12:    Inject recorded wavefield energy in  $\mathcal{D}^\dagger(x, z = 0, t)$  into  $\mathcal{R}^\dagger(x, z, t)$ 
13:    Reconstruct  $\mathcal{R}^\dagger(x, z, t - \Delta t)$  from  $\mathcal{R}^\dagger(x, z, t)$  and  $\mathcal{R}^\dagger(x, z, t + \Delta t)$ 
14:    Reconstruct  $\mathcal{S}(x, z, t - \Delta t)$  and  $\mathcal{S}(x, z, t + \Delta t)$ 
15:    Apply imaging condition in Eq. (5)
16:  end for
17: end for
18: Sum images formed by each source

```

wavefield encounters a reflector, each point on the reflector acts as the source of a new, scattered wavefield.⁴³ That is, the time when a downward-propagating “source” wavefield is incident on a reflector is temporally and spatially coincident with the upward-propagating, scattered wavefield (the wavefield “received” at the surface). RTM aims to determine the location and time where and when these two wavefields are collocated through an imaging condition. As in the numerical experiment in Sec. 2.1, we generate and numerically propagate a source wavefield $\mathcal{S}(x, z, t)$ through the acoustic model using the SPEC-FEM2D software. The interactions of the source wavefield with an acoustic discontinuity (the circular vessel) generate a scattered wavefield $\mathcal{R}(x, z, t)$. The scattered wavefield subsequently propagates to the surface where it is recorded and extracted as data $\mathcal{D}(x, z = 0, t)$ as in Fig. 1(c).

The first step in RTM is to reconstruct wavefields $\mathcal{S}(x, z, t)$ and $\mathcal{R}^\dagger(x, z, t)$. Numerically speaking, the \dagger symbol indicates that a wavefield is formed by injecting energy in an acausal way (from t_{\max} to $t = 0$). First, we reconstruct $\mathcal{S}(x, z, t)$ by generating a numerical approximation of the source wavelet, and propagating it through the model from $t = t_0 = 0$ to $t = t_{\max}$ using the FDTD approach described in Appendix A1. Having established the source wavefield at t_{\max} , we time-reverse the

wavefield and begin to evolve $\mathcal{S}(x, z, t)$ in reverse time from $t = t_{\max}$ to $t = t_0$. At each time step, we also inject the recorded, time-reversed data $\mathcal{D}^\dagger(x, z = 0, t)$ into the initialized receiver wavefield $\mathcal{R}^\dagger(x, z, t)$ at t_{\max} . Then, to facilitate imaging, we simultaneously back-propagate $\mathcal{S}(x, z, t)$ and $\mathcal{R}^\dagger(x, z, t)$ from t_{\max} to t_0 . We image an acoustic scatterer or reflector when there is high correlation between $\mathcal{R}^\dagger(x, z, t)$ and $\mathcal{S}(x, z, t)$. We describe this process explicitly in Algorithm 1 and demonstrate with the numerical ultrasound model in Fig. 8.

The cross-correlation step (15) forms an image $I(x, z)$ using a cross-correlation imaging condition⁶¹

$$I(x, z) = \sum_{s=1}^N \sum_{t=0}^{t_{\max}} \mathcal{S}(x, z, t) \mathcal{R}^\dagger(x, z, t), \quad (5)$$

where N is the number of independent sources (or shot-gathers) and \dagger indicates time reversal. $\mathcal{R}^\dagger(x, z, t)$ will focus at the location of an acoustic target at the time it was scattered. Likewise, $\mathcal{S}(x, z, t)$ will require the same time to reach the target. When the energy in $\mathcal{S}(x, z, t)$ and $\mathcal{R}^\dagger(x, z, t)$ is collocated in space and time, the cross-correlation imaging condition will form an image of acoustic reflectivity at the corresponding location;

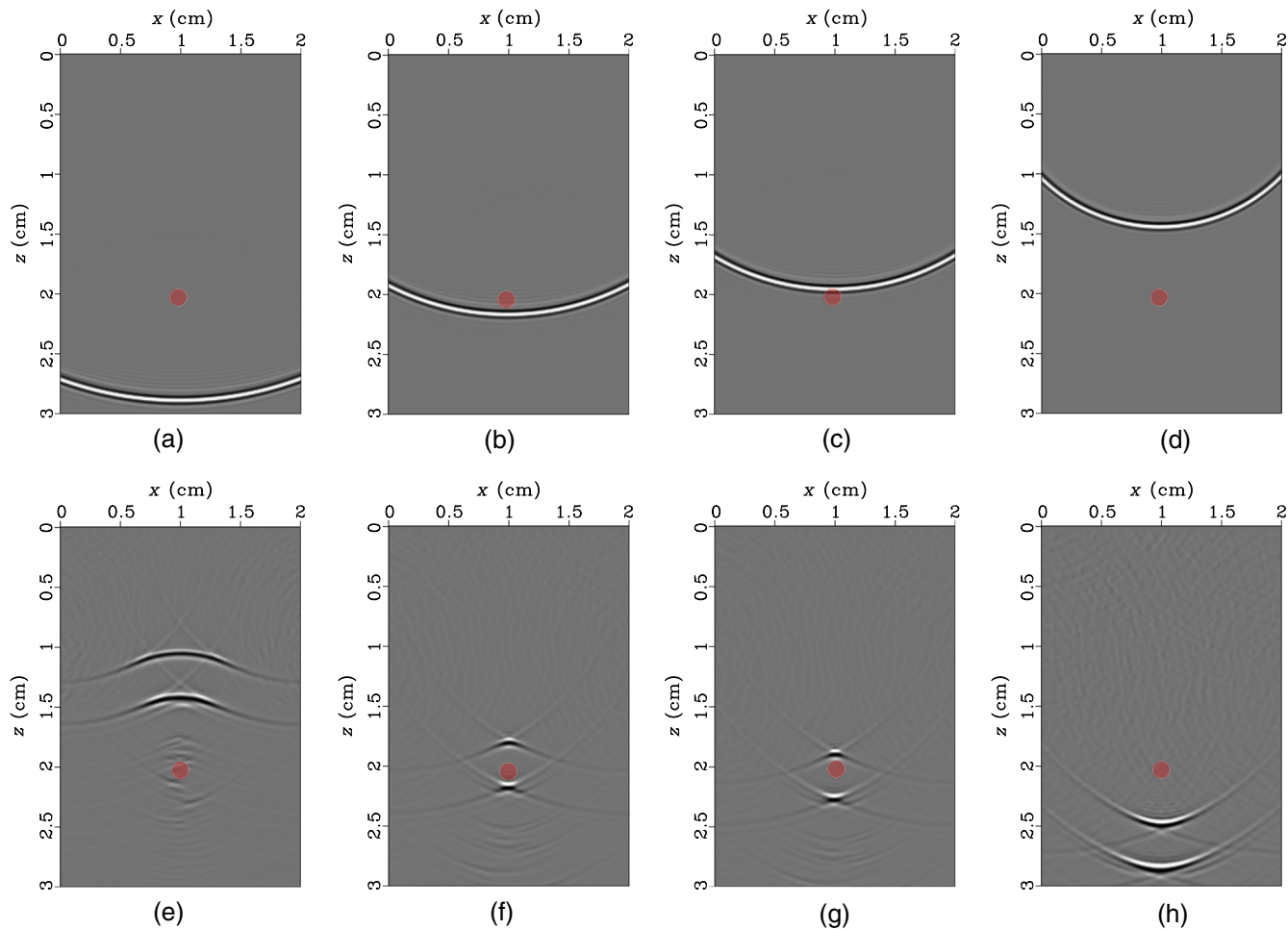


Fig. 8 Snapshots of the process of RTM to image the walls of a vessel in simulated data. The top panels show the numerical source wavefield $\mathcal{S}(x, z, t)$ back-propagating from deep within the model. The bottom panels are the back-propagation of the scattered wavefield injected into the model backward in time $\mathcal{R}^\dagger(x, z, t)$. The snapshots are shown from left to right in the order they are performed. An image is formed when $\mathcal{S}(x, z, t)$ and $\mathcal{R}^\dagger(x, z, t)$ are collocated in space and time, as shown in the middle two panels.

Algorithm 2 Time-reversal for PA imaging.

-
- 1: Reverse-time axes of PA data $\mathcal{D}^\dagger(x, t)$
 - 2: Set $\mathcal{R}^\dagger(x, z, t_{\max} + \Delta t) = 0$
 - 3: **for** $t_{\max} > t > t_0$ **do**
 - 4: Inject $\mathcal{D}^\dagger(x, z = 0, t)$ into receiver wavefield $\mathcal{R}^\dagger(x, z, t)$
 - 5: Reconstruct $\mathcal{R}^\dagger(x, z, t - \Delta t)$ from $\mathcal{R}^\dagger(x, z, t)$ and $\mathcal{R}^\dagger(x, z, t + \Delta t)$
 - 6: **end for**
 - 7: Extract wavefield at final time-step, $\mathcal{R}^\dagger(x, z, t = t_0)$
-

that is, the image is formed when $\mathcal{R}^\dagger(x, z, t)$ and $\mathcal{S}(x, z, t)$ “pass” each other (see Fig. 8).

A2 Photoacoustic Reconstruction with Time-Reversal

To reconstruct the PA image, we assume a homogeneous background medium and propagate the recorded PA wavefield backward in time as in Algorithm 2. The image is formed by extracting the wavefield at time $t = t_0$, when the light was triggered.

Disclosures

The authors of this article have no conflicts of interest to disclose.

Acknowledgments

This work was supported by a 2014 Research Collaboration Award from the University of Western Australia. We would also like to acknowledge the Madagascar software package for multidimensional analysis and reproducible computational experiments.

References

1. F. Duck, *Physical Properties of Tissues: A Comprehensive Reference Book*, Academic Press Limited, San Diego, California (1990).
2. P. Beard, “Biomedical photoacoustic imaging,” *Interface Focus* **1**(4), 602–631 (2011).
3. R. G. Kolkman et al., “Real-time *in vivo* photoacoustic and ultrasound imaging,” *J. Biomed. Opt.* **13**(5), 050510 (2008).
4. X. Wang et al., “Photoacoustic imaging with a commercial ultrasound system and a custom probe,” *Ultrasound Med. Biol.* **37**(3), 484–492 (2011).
5. R. W. Speirs and A. I. Bishop, “Photoacoustic tomography using a Michelson interferometer with quadrature phase detection,” *Appl. Phys. Lett.* **103**, 053501 (2013).
6. G. Rousseau et al., “Non-contact biomedical photoacoustic and ultrasound imaging,” *J. Biomed. Opt.* **17**(6), 061217 (2012).
7. A. Hochreiner et al., “Photoacoustic imaging using an adaptive interferometer with a photorefractive crystal,” *J. Biophotonics* **5**(7), 508–517 (2012).
8. E. Zhang, J. Laufer, and P. Beard, “Backward-mode multiwavelength photoacoustic scanner using a planar Fabry-Perot polymer film ultrasound sensor for high-resolution three-dimensional imaging of biological tissues,” *Appl. Opt.* **47**(4), 561–577 (2008).
9. T. Ling, S.-L. Chen, and L. J. Guo, “Fabrication and characterization of high Q polymer micro-ring resonator and its application as a sensitive ultrasonic detector,” *Opt. Express* **19**(2), 861–869 (2011).
10. A. Rosenthal, D. Razansky, and V. Ntziachristos, “High-sensitivity compact ultrasonic detector based on a pi-phase-shifted fiber Bragg grating,” *Opt. Lett.* **36**(10), 1833–1835 (2011).
11. R. A. Barnes et al., “Probe beam deflection technique as acoustic emission directionality sensor with photoacoustic emission source,” *Appl. Opt.* **53**(3), 511–519 (2014).
12. M. E. Khosroshahi and A. Mandelis, “Combined photoacoustic ultrasound and beam deflection signal monitoring of gold nanoparticle agglomerate concentrations in tissue phantoms using a pulsed Nd:YAG laser,” *Int. J. Thermophys.* **36**(5), 880–890 (2015).
13. J. L. Johnson et al., “Gas-coupled laser acoustic detection as a non-contact line detector for photoacoustic and ultrasound imaging,” *J. Opt.* **18**(2), 024005 (2016).
14. S. Manohar et al., “Concomitant speed-of-sound tomography in photoacoustic imaging,” *Appl. Phys. Lett.* **91**(13), 131911 (2007).
15. J. Xia et al., “Enhancement of photoacoustic tomography by ultrasonic computed tomography based on optical excitation of elements of a full-ring transducer array,” *Opt. Lett.* **38**(16), 3140–3143 (2013).
16. S. A. Ermilov et al., “Three-dimensional laser photoacoustic and laser ultrasound imaging system for biomedical research,” *Proc. SPIE* **9323**, 93230N (2015).
17. S.-Y. Hung et al., “Concurrent photoacoustic-ultrasound imaging using single-laser pulses,” *J. Biomed. Opt.* **20**(8), 086004 (2015).
18. A. Conjuteau et al., “Measurement of the spectral directivity of photoacoustic and ultrasonic transducers with a laser ultrasonic source,” *Rev. Sci. Instrum.* **80**(9), 093708 (2009).
19. G. Rousseau, A. Blouin, and J.-P. Monchalain, “Non-contact photoacoustic tomography and ultrasonography for tissue imaging,” *Biomed. Opt. Express* **3**(1), 16–25 (2012).
20. G. Bal and K. Ren, “Multi-source quantitative photoacoustic tomography in a diffusive regime,” *Inverse Prob.* **27**(7), 075003 (2011).
21. B. Cox, T. Tarvainen, and S. Arridge, “Multiple illumination quantitative photoacoustic tomography using transport and diffusion models,” in *Contemporary Mathematics: Tomography and Inverse Transport Theory*, G. Bal et al., Eds., Vol. **559**, Chapter 1, American Mathematical Society, Providence, Rhode Island (2011).
22. D. Finch and S. K. Patch, “Determining a function from its mean values over a family of spheres,” *SIAM J. Math. Anal.* **35**(5), 1213–1240 (2004).
23. Y. Xu and L. V. Wang, “Time reversal and its application to tomography with diffracting sources,” *Phys. Rev. Lett.* **92**(3), 033902 (2004).
24. P. Burgholzer et al., “Exact and approximative imaging methods for photoacoustic tomography using an arbitrary detection surface,” *Phys. Rev. E* **75**(4), 046706 (2007).
25. B. Cox and P. Beard, “Photoacoustic tomography with a single detector in a reverberant cavity,” *J. Acoust. Soc. Am.* **125**(3), 1426–1436 (2009).
26. B. T. Cox and B. E. Treeby, “Artifact trapping during time reversal photoacoustic imaging for acoustically heterogeneous media,” *IEEE Trans. Med. Imaging* **29**(2), 387–396 (2010).
27. E. Bossy et al., “Time reversal of photoacoustic waves,” *Appl. Phys. Lett.* **89**(18), 184108 (2006).
28. Y. Hristova, P. Kuchment, and L. Nguyen, “Reconstruction and time reversal in thermoacoustic tomography in acoustically homogeneous and inhomogeneous media,” *Inverse Prob.* **24**(5), 055006 (2008).
29. H. Grün et al., “Photoacoustic tomography of heterogeneous media using a model-based time reversal method,” *Proc. SPIE* **6856**, 685620 (2008).
30. B. E. Treeby, E. Z. Zhang, and B. Cox, “Photoacoustic tomography in absorbing acoustic media using time reversal,” *Inverse Prob.* **26**(11), 115003 (2010).
31. E. Baysal, D. D. Kosloff, and J. W. Sherwood, “Reverse time migration,” *Geophysics* **48**(11), 1514–1524 (1983).
32. N. D. Whitmore, “Iterative depth migration by backward time propagation,” in *1983 SEG Annual Meeting*, Society of Exploration Geophysicists (1983).
33. B. Arnal, M. Pernot, and M. Tanter, “Experimental reverse time migration for imaging of elasticity changes,” in *IEEE Ultrasonics Symp. (IUS '10)*, pp. 1039–1042, IEEE (2010).
34. O. Roy et al., “Ultrasound breast imaging using frequency domain reverse time migration,” *Proc. SPIE* **9790**, 97900B (2016).
35. K. E. Thomenius, “Evolution of ultrasound beamformers,” in *Proc., IEEE Ultrasonics Symp.*, Vol. **2**, pp. 1615–1622, IEEE (1996).

36. J. A. Jensen et al., "Synthetic aperture ultrasound imaging," *Ultrasonics* **44**, e5–e15 (2006).
37. S. K. Jespersen, J. E. Wilhjelm, and H. Sillesen, "Multi-angle compound imaging," *Ultrason. Imaging* **20**(2), 81–102 (1998).
38. D. Connolly, L. Berman, and E. McNally, "The use of beam angulation to overcome anisotropy when viewing human tendon with high frequency linear array ultrasound," *Br. J. Radiol.* **74**(878), 183–185 (2001).
39. C. Geuzaine and J.-F. Remacle, "Gmsh: a 3-D finite element mesh generator with built-in pre- and post-processing facilities," *Int. J. Numer. Methods Eng.* **79**(11), 1309–1331 (2009).
40. H. A. Afifi, "Ultrasonic pulse echo studies of the physical properties of PMMA, PS, and PVC," *Polym.-Plast. Technol. Eng.* **42**(2), 193–205 (2003).
41. J. L. Johnson, K. Van Wijk, and M. Sabick, "Characterizing phantom arteries with multi-channel laser ultrasonics and photo-acoustics," *Ultrasound Med. Biol.* **40**(3), 513–520 (2014).
42. J. Tromp, D. Komatitsch, and Q. Liu, "Spectral-element and adjoint methods in seismology," *Commun. Comput. Phys.* **3**(1), 1–32 (2008).
43. J. A. Scales, *Theory of Seismic Imaging*, Vol. **55**, Springer-Verlag, Berlin (1995).
44. *American National Standard for Safe Use of Lasers: Z136.1*, Laser Institute of America, Orlando, Florida (2007).
45. R. Cubeddu et al., "A solid tissue phantom for photon migration studies," *Phys. Med. Biol.* **42**(10), 1971–1979 (1997).
46. J. L. Johnson, H. Tom Wörden, and K. Van Wijk, "PLACE: an open-source python package for laboratory automation, control, and experimentation," *J. Lab. Autom.* **20**(6), 10–16 (2015).
47. J. Jose et al., "Speed-of-sound compensated photoacoustic tomography for accurate imaging," *Med. Phys.* **39**(12), 7262–7271 (2012).
48. C. Huang et al., "Joint reconstruction of absorbed optical energy density and sound speed distributions in photoacoustic computed tomography: a numerical investigation," *IEEE Trans. Comput. Imaging* **2**(2), 136–149 (2016).
49. T. P. Matthews et al., "Synergistic image reconstruction for hybrid ultrasound and photoacoustic computed tomography," *Proc. SPIE* **9323**, 93233A (2015).
50. G. Li et al., "Multiview Hilbert transformation for full-view photoacoustic computed tomography using a linear array," *J. Biomed. Opt.* **20**(6), 066010 (2015).
51. C. B. Scruby and L. E. Drain, *Laser Ultrasonics: Techniques and Applications*, Adam Hilger, Bristol (1990).
52. J. Gateau et al., "Improving visibility in photoacoustic imaging using dynamic speckle illumination," *Opt. Lett.* **38**(23), 5188–5191 (2013).
53. K. Wapenaar et al., "Three-dimensional single-sided marchenko inverse scattering, data-driven focusing, greens function retrieval, and their mutual relations," *Phys. Rev. Lett.* **110**(8), 084301 (2013).
54. G. Dutta and G. T. Schuster, "Attenuation compensation for least-squares reverse time migration using the viscoacoustic-wave equation," *Geophysics* **79**(6), S251–S262 (2014).
55. Y. Zhang and J. Sun, "Practical issues in reverse time migration: true amplitude gathers, noise removal and harmonic source encoding," *First Break* **26**, 29–35 (2009).
56. J. Laufer et al., "Quantitative spatially resolved measurement of tissue chromophore concentrations using photoacoustic spectroscopy: application to the measurement of blood oxygenation and haemoglobin concentration," *Phys. Med. Biol.* **52**(1), 141–168 (2007).
57. B. E. Anderson et al., "Improving spatio-temporal focusing and source reconstruction through deconvolution," *Wave Motion* **52**, 151–159 (2015).
58. B. Cox and P. C. Beard, "Modelling photoacoustic propagation in tissue using k-space techniques," in *Photoacoustic Imaging and Spectroscopy*, L. V. Wang, Ed., Chapter 3, Taylor and Francis, Boca Raton, Florida (2009).
59. J. Shragge, "Solving the 3D acoustic wave equation on generalized structured meshes: a finite-difference time-domain approach," *Geophysics* **79**(6), T363–T378 (2014).
60. R. M. Weiss and J. Shragge, "Solving 3D anisotropic elastic wave equations on parallel GPU devices," *Geophysics* **78**(2), F7–F15 (2013).
61. J. F. Claerbout, "Toward a unified theory of reflector mapping," *Geophysics* **36**(3), 467–481 (1971).

Jami L Johnson is a PhD candidate in the Physics Department at the University of Auckland. She received her BSc in physics from Bethel University in St. Paul, Minnesota, in 2011 and her MSc in mechanical engineering from Boise State University, Idaho, in 2013. Her current research interests include all-optical photoacoustic and laser-ultrasound imaging for biomedical applications.

Jeffrey Shragge is a Woodside professor in computational geoscience at the University of Western Australia. He received his BScH in physics from Queen's University in 1998, and his MSc in teleseismic imaging from the University of British Columbia in 2001. From 2001 to 2002, he worked for a geophysical consulting company based in Woburn, Massachusetts. He graduated with his PhD in geophysics from the Stanford Exploration Project in 2009. His research interests are seismic imaging/inversion, wave propagation, and high-performance computing.

Kasper van Wijk is an associate professor in the Physics Department at the University of Auckland. His current research interests are in laser-ultrasonics, seismology, and elastic wave propagation. He works on a wide variety of applications, ranging from remotely sensing the structure of the Earth's subsurface with scattered seismic waves, to exciting and detecting ultrasonic waves with lasers in (fractured) earth, composite, and biological materials in the Physical Acoustics Laboratory.